Table S1. Quantification of active replication foci, related to Figure 1

	Microscopy	Cell model	Label	Replication foci density	Number of replication foci
This work	STORM	U2OS	PCNA	$4.7 \pm 1.6\ \mu m^{-2}$	$(3.7 \pm 1.3) \times 10^3$ [a]
Su et al., 2020	STORM	HeLa-S3	EdU	$1.5\sim2\ \mu m^{-2}$	$(1.2 \sim 1.6) \times 10^3$ [a]
Chagin et al., 2016	3D-SIM	HeLa-Kyoto	PCNA	NA	$(5.2 \pm 2.1) \times 10^3$
Baddeley et al., 2009	3D-SIM	C2C12	BrdU	NA	$(6.4 \pm 0.7) \times 10^3$
Cseresnyes et al., 2009	STED	MRC5	PCNA	$\sim4.1\ \mu m^{-3}$	$\sim1.6 \times 10^3$ [b]

NT	$4.7 \pm 1.6\ \mu m^{-2}$ (N=1863)[c]		[HU] (μM)	NT	ATRi
ATRi	$5.4 \pm 1.8\ \mu m^{-2}$ (N=1267)		0	$4.7 \pm 1.6\ \mu m^{-2}$ (N=1863)	$5.4 \pm 1.8\ \mu m^{-2}$ (N=1267)
CDC7i	$3.9 \pm 1.5\ \mu m^{-2}$ (N=470)		50	$4.6 \pm 1.5\ \mu m^{-2}$ (N=343)	$4.4 \pm 1.5\ \mu m^{-2}$ (N=248)
CDC7i+ATRi	$3.9 \pm 1.7\ \mu m^{-2}$ (N=933)		500	$3.7 \pm 1.5\ \mu m^{-2}$ (N=306)	$4.4 \pm 1.7\ \mu m^{-2}$ (N=241)

a: data is propagated from the foci density by assuming that 1) the volume of the nucleus is about $\pi\times(10/2)^2\times5\ \mu m^3$ and that 2) the 2D imaging depth is ~ 0.5 μm;
b: data is propagated from the foci density by assuming that the volume of the nucleus is about $\pi\times(10/2)^2\times5\ \mu m^3$;
c: mean ± SD, N indicates number of ROI region (~6×6 μm^2).

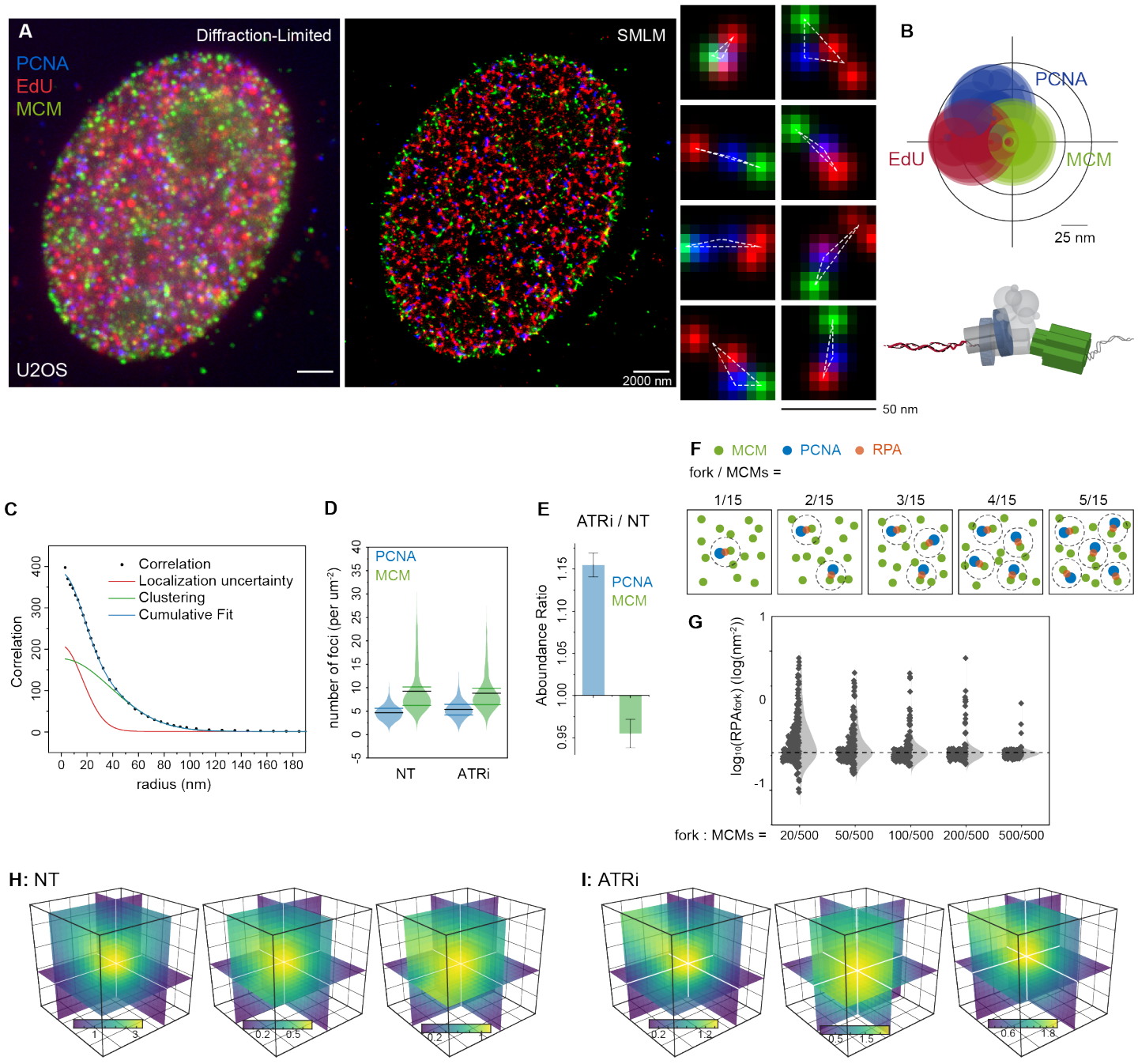

Figure S1. Quantification of the organization of individual replisomes in cells. Related to Figure 1.

(A) A representative Diffraction-Limited fluorescence microscopy image and its corresponding reconstructed SMLM image of a cell showing PCNA, MCM and nascent DNA (EdU). EdU was pulsed for 15 minutes prior to harvest, and detected with AlexaFluor647-azid via the click reaction. Side panels shows representative magnified images of individual replisomes and their patterns.

(B) Overlaid EdU-PCNA-MCM TCF-resolved single-replisome configurations from SMLM images of single cells (N = 54 nuclei). The EdU-MCM edges of all the triangular patterns were aligned to the same horizontal with a fixed position of MCM.

(C-E) Estimate of the number of active replication forks (see Methods S4). Representative Auto Correlation Function (ACF) profile of the SMLM image of PCNA. The average density of the fluorophores across the ROI and the average number of

the fluorophores of each PCNA focus can be derived from the fitting of the ACF(Sengupta et al., 2011; Veatch et al., 2012). The density of the PCNA foci across the ROI was then estimated by dividing the average number of the fluorophores of each PCNA focus from the average density of the fluorophores across the ROI.

(D) Quantification of the levels of PCNA and MCM foci density reveals that the MCM is much more abundant than PCNA (twice the amount). This is anticipated since more MCMs are loaded on chromatin, and reside not only at active replication foci but also at unfired and dormant origins. Mean values and the 1st and 3rd quartile were marked as black and colored bars, respectively, N = 1863 and 1267 cells for NT and ATRi, respectively.

(E) Quantification of the abundance ratio between data as indicated. Error bars in is the propagated SEM.

(F and G) Validation of the TCF analyses via simulated SMLM data. As shown in the simulation scheme (F), a large number of MCMs (green) are randomly distributed across the canvas; Some of the MCMs are placed at the lead of an active replication fork with PCNA (blue) and RPA (red). Each active fork is simulated as a relatively flexible configuration, with $BG = 40 \pm 2$, $BR = 20 \pm 1$, and $\angle GBR = 0 \pm \pi/8$ (mean ± std for normal distribution sampling). Once each fork triangle is formed, a dihedral between the triangle plane and the 'imaging' plane was randomly sampled within $[-\pi/2,\ \pi/2]$. The triangle was then projected to its 'imaging' plane for TCF analyses.

(G) TCF based quantification of active forks is unaffected by abundance of MCM. Simulation where 500 MCMs in total were seeded onto a canvas with different number of active forks as indicated. 200 simulation repeats were performed for statistics.

(H and I) Representative TCF profiles for NT (H) and ATRi (I), indicating a similar dispersion of the TCF profile. We note that the dispersion of the TCF profile is attributed to the structural fluctuations of the replisome, the localization accuracy, the chromatic aberration (see Methods S3), and the projection of 3D configuration to the 2D imaging plane. However, as the sample preparations was consistent across different experimental conditions, the dispersions display similar range, and thus does not affect the interpretation of the data.

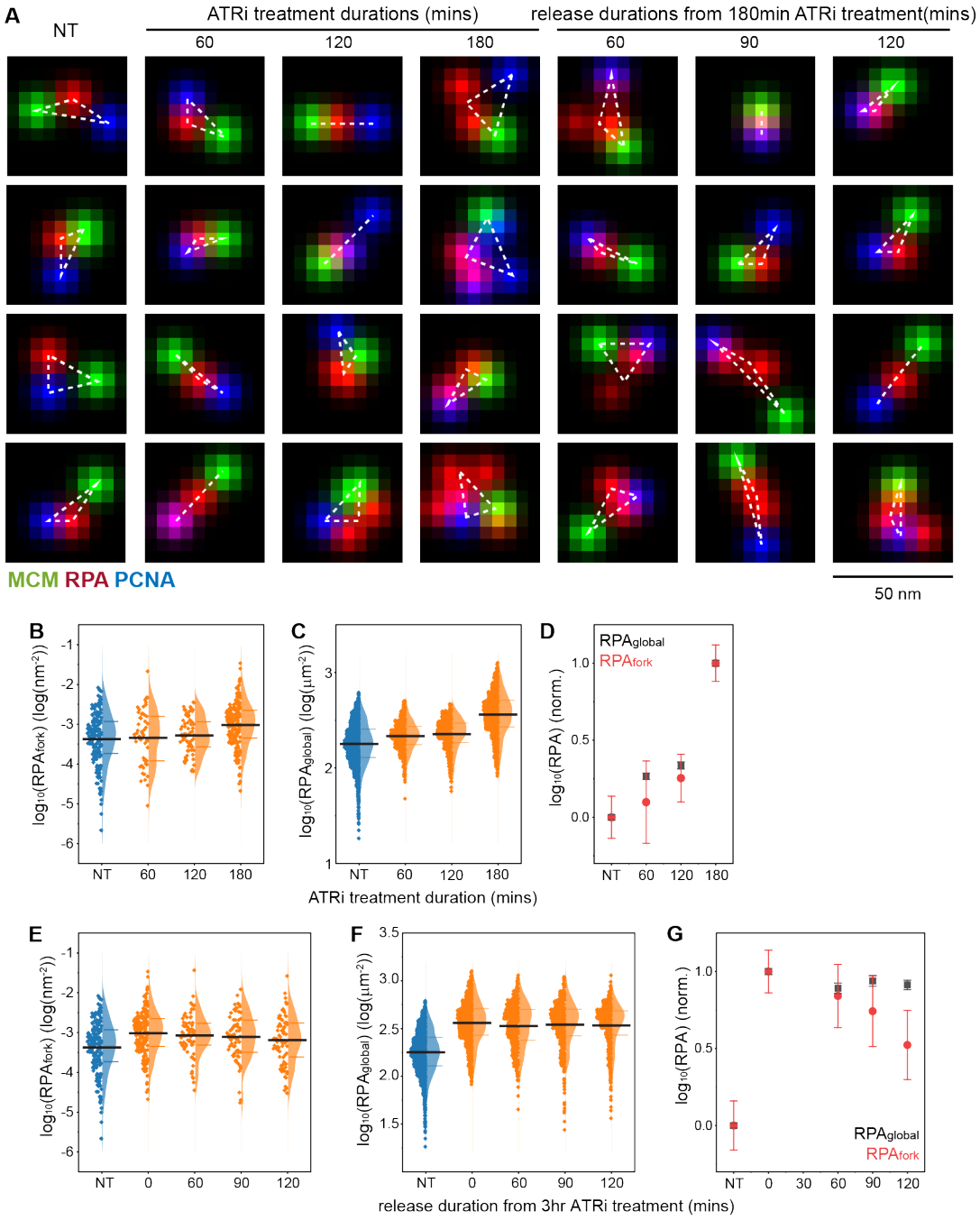

Figure S2. Kinetics of ATRi-induced RPA fork accumulation (RPA_{fork}) and origin firing (RPA_{global}). Related to Figure 1.

(A) Representative images of single replisomes. Four replisomes are shown per column, where each column correspond to a different experimental condition.

(B and C) Quantifications of the level of RPA_{fork} (B) and RPA_{global} (C) with different ATRi treatment duration. Mean and the 1st and 3rd quartile were labeled as black and colored bars. N = 193, 53, 70, and 177 for NT, 60, 120, and 180-minute treatment in (B), N = 1863, 561, 533, and 1267 for NT, 60, 120, 180-minute treatment in (C).

(D) Normalized Mean ± SEM of data in (B) and (C), indicating similar activation kinetics.

(E and F) Quantifications of the level of RPA_{fork} (E) and RPA_{global} (F) with different release durations from 3-hour ATRi treatment. Mean and the 1st and 3rd quartile were labeled as black and colored bars. N = 193, 177, 72, 68, and 79 for NT, 0, 60, 90, 120-minute release in (E), N = 1863, 1267, 512, 528, and 575 for NT, 0, 60, 90, 120-minute release in (F).

(G) Normalized Mean ± SEM of data in (E) and (F), indicating a slightly different kinetics of reactivation of ATR activities.

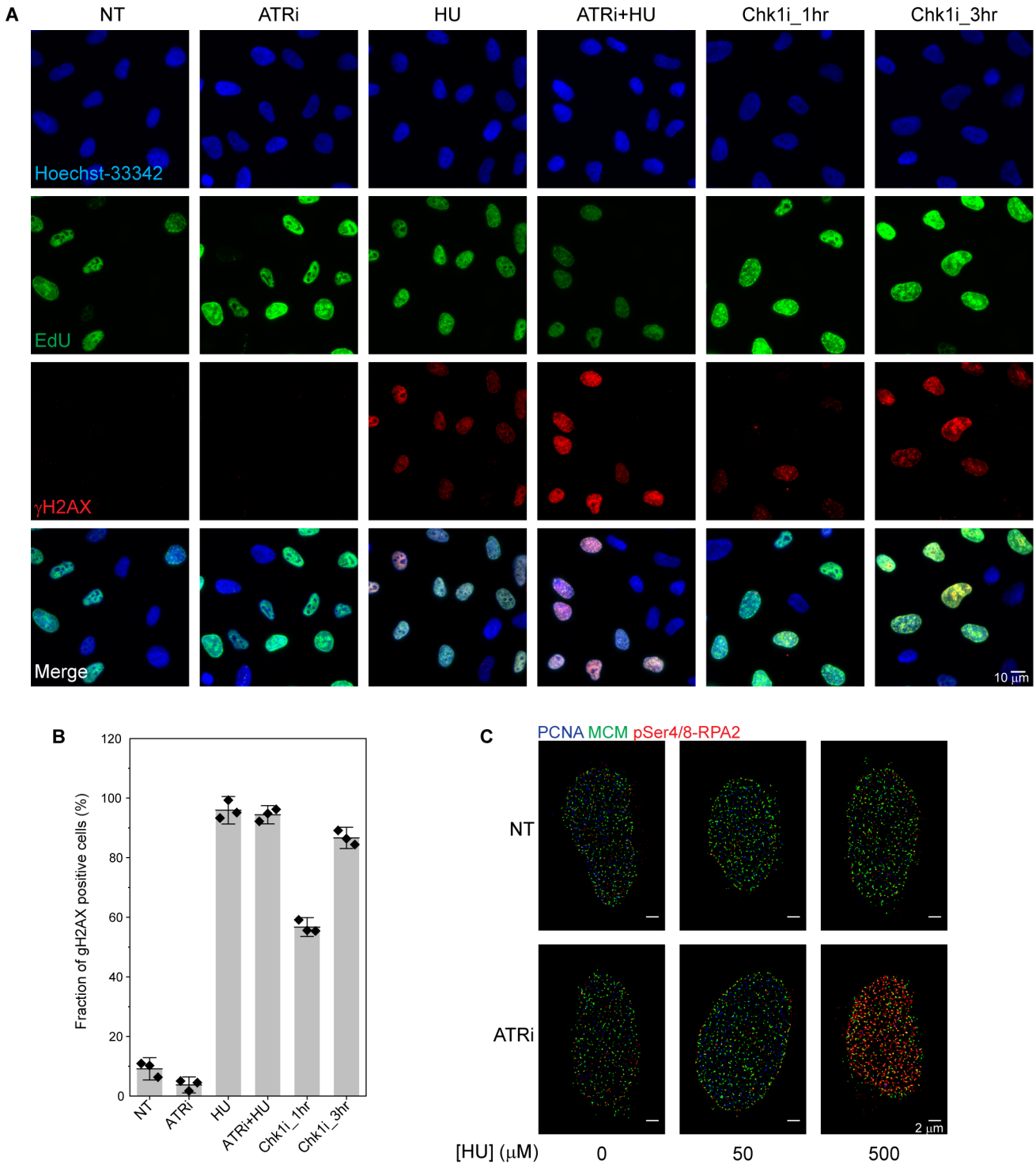

Figure S3. Inhibition of ATR does not result in immediate DNA damage at replication forks. Related to Figure 1.

(A) Analysis of DNA damage resulting from treatment with HU, ATRi and Chk1i via epifluorescence microscopy. Cells were pulsed with EdU (10 μM, 3h) to identify S-phase cells, and immunostained for the DNA damage marker, γH2AX (red) for the different treatments as indicated (STAR Methods). EdU (green) was detected with AlexaFluor488-azide via click chemistry and DNA was counterstained with Hoechst-33342 (blue) for nucleus marker.

(B) Quantification of the percentage S phase cells with > 15 γH2AX foci. Mean ± SEM, N = 3 experimental repeats.

(C) Representative SMLM images of S-phase cells that were also stained for pRPA-Ser4/8, under different ATRi and HU treatments as indicated. Emergence of pRPA-Ser4/8 signal as marker of DNA damage was only detected when induction of moderate replication stress ([HU] = 500 μM) was combined with ATRi treatment.

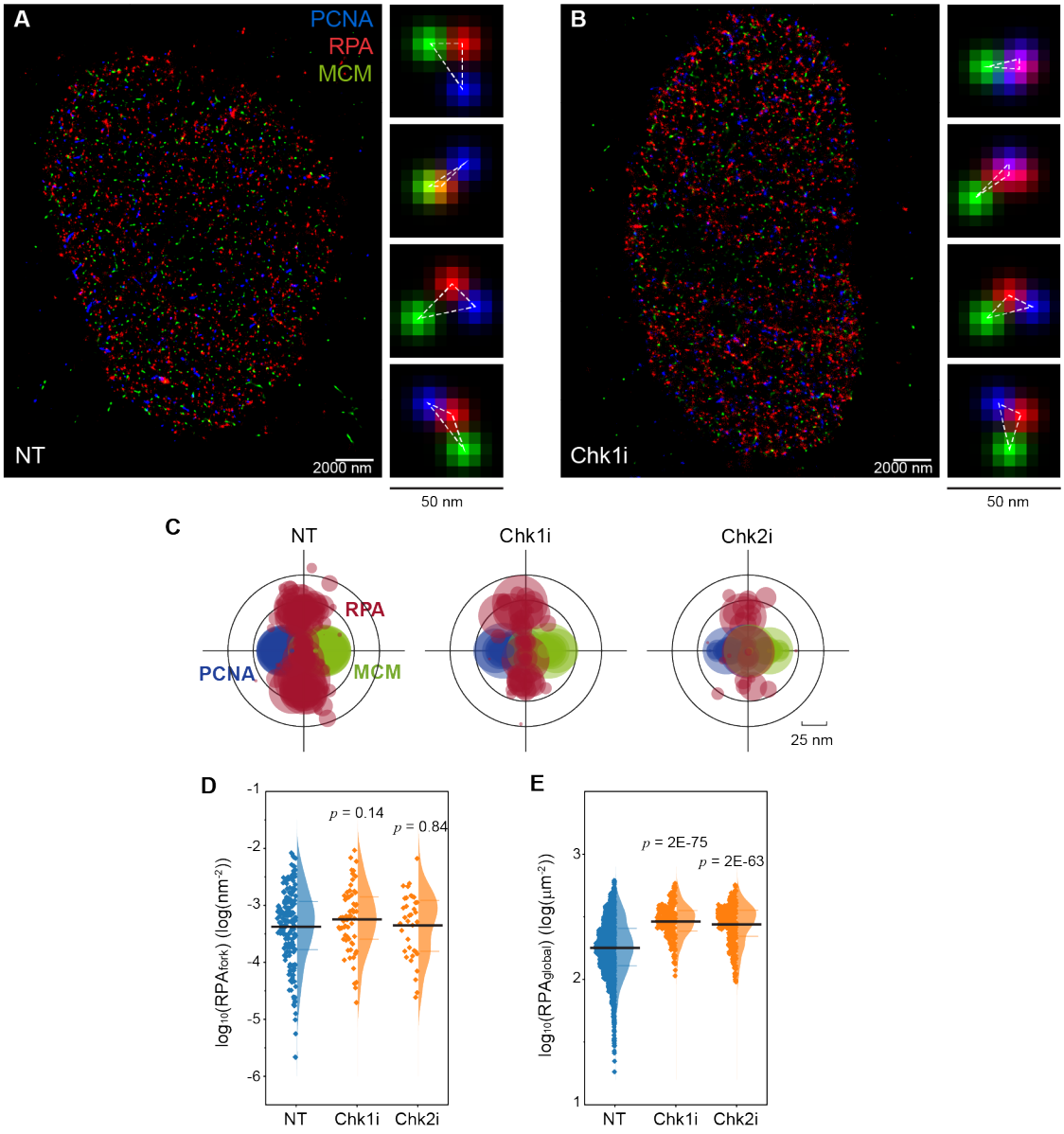

Figure S4. Inhibition of Chk1 does not lead to accumulation of RPA at forks. Related to Figure 2.

(A and B) Representative SMLM images of replication fork factors PCNA, RPA, and MCM in S phase cells with non-treatment (A) or treated with Chk1i (B). Magnified panels for each image show representative triplet patterns of individual replications forks.

(C) Overlaid PCNA-RPA-MCM TCF-resolved single-replisome configurations from SMLM images of single cells under different treatments. Circle size represents the average density of RPA at each fork within a nucleus.

(D) Quantifications of the levels of RPA_{fork} for the TCF-resolved single-replisome configurations shown in (C) at different treatment conditions. Mean values and the 1st and 3rd quartile were marked as black and colored bars, respectively, N = 193, 61, and 36 for NT, Chk1i, and Chk2, respectively.

(E) Quantifications of the levels of RPA_{global} within each single cell at different treatment conditions. Mean values and the 1st and 3rd quartile were marked as black and colored bars, respectively, N = 1863, 261, and 369 for NT, Chk1i, and Chk2, respectively.

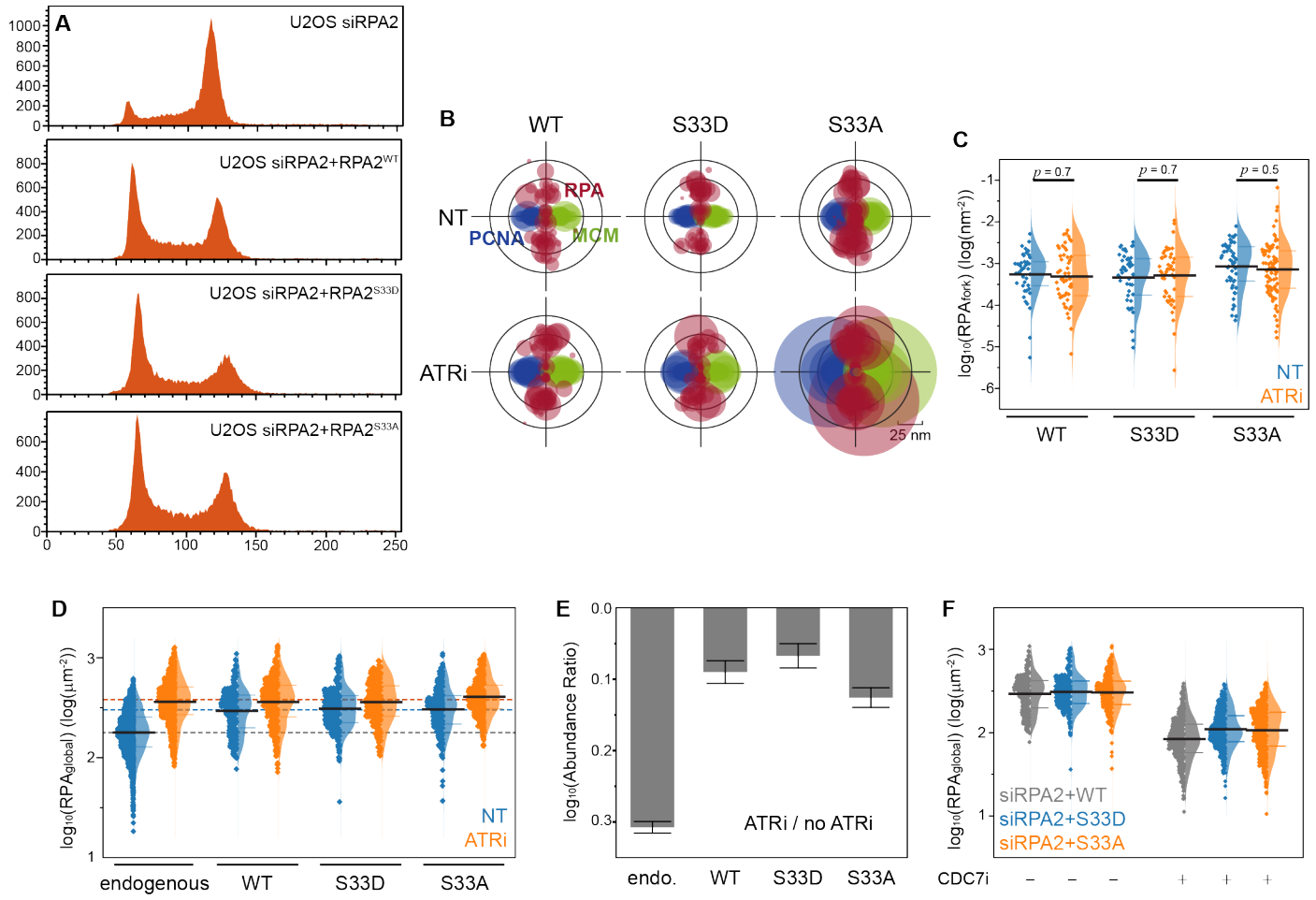

Figure S5. Substitution of the endogenous RPA2 with transfected wild-type or mutant RPA2 does not impact replication or cell cycle. Related to Figure 4.

(A) Flow cytometry analyses of U2OS cells with RPA2 largely depleted and supplemented with different exogenous RPA2 as indicated.

(B) Overlaid PCNA-RPA-MCM TCF-resolved single-replisome configurations from SMLM images of single cells under different treatments. Circle size represents the average density of RPA at each fork within a nucleus.

(C) Quantifications of the levels of RPA_{fork} for the TCF-resolved single-replisome configurations shown in (B) with different treatments. Mean and the 1st and 3rd quartile were labeled as black and colored bars, respectively, N = 43, 52, 48, 49, 52, and 85 for WT-NT, WT-ATRi, S33D-NT, S33D-ATRi, S33A-NT, and S33A-ATRi, respectively.

(D and E) Quantifications of the levels of RPA_{global} within each single cell with different treatments. Mean and the 1st and 3rd quartile were labeled as black and colored bars, respectively, N = 1863, 1267, 339, 474, 374, 258, 389, and 517 for endo-NT, endo-ATRi, WT-NT, WT-ATRi, S33D-NT, S33D-ATRi, S33A-NT, and S33A-ATRi, respectively. The abundance ratio between data with ATRi treatment and w/o ATRi treatment is displayed in (E), Error bars in (E) are propagated SEM. We note that ATRi treatment of RPA2 complemented cells following RPA2 depletion did not lead to accumulation of the transfected RPA at forks at the levels observed in the WT cells (Figure S5B and S5C), and transfected cells also displayed higher level of origin firing than that of the WT cells (Figure S5D and S5E), suggesting that the expression of the exogenous RPAs does not fully recover ATR's activity that was suppressed via RPA2 depletion beforehand.

(F) Quantifications of the levels of RPA_{global} within each single cell under different treatments. Mean values and the 1st and 3rd quartile were marked as black and colored bars, respectively, N = 339, 374, 389, 477, 475, and 619 for WT-CDC7i-, S33D-CDC7i-, S33A-CDC7i-, WT-CDC7i+, S33D-CDC7i+, and S33A-CDC7i+, respectively. Note that RPA_{global} is substantially reduced by CDC7i which largely suppresses the excessive origin firing caused by the disrupted ATR activity (B - E) in the transfected cells.

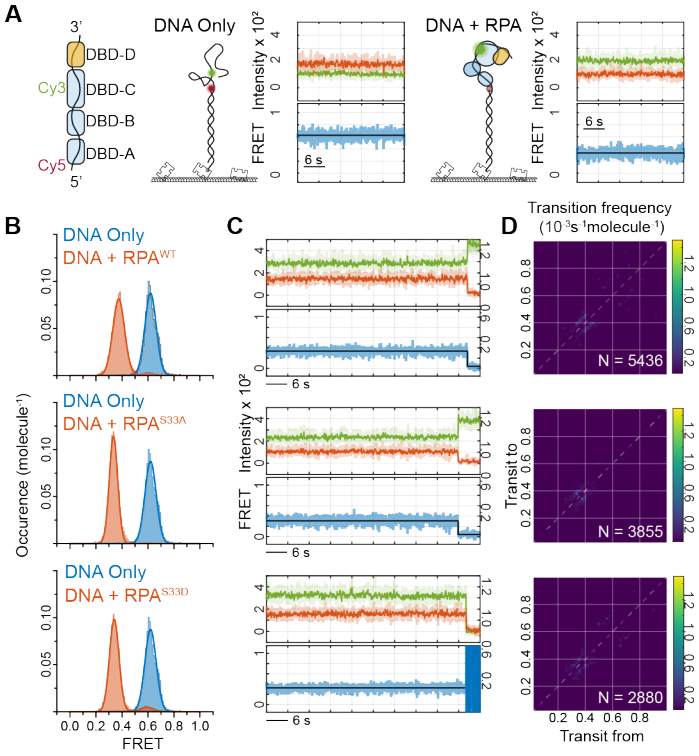

Figure S6. Phosphorylation of RPA2 at Ser33 does NOT affect the binding coordination between RPA1 and ssDNA. Related to Figure 5.

(A) Schematic representation of RPA binding coordination on ssDNA monitored by smFRET. The Cy5 was at the 5'-end and positioned at the duplex junction of the partial duplex construct with a 32nt-long ssDNA, with the Cy3 located at the ssDNA 16 nt away, so that the changes in FRET efficiency represents whether RPA1 binds to the ssDNA.

(B) FRET histograms showing ssDNA bound with different RPA mutants as indicated (Red) as compared to DNA only (blue).

(C) Representative single-molecule trajectories of ssDNA bound by different RPA mutants as indicated.

(D) The Transition Density Plot (TDP) attained from the smFRET trajectories of ssDNA bound by different RPA mutants. The TDP heat map applied the same scale as in Figure 5E.

Methods S1. The Triple-Correlation-Function (TCF)

In this study we applied an established automated analysis pipeline, which is described in great detail and demonstrated in previous studies (Lee et al., 2021; Yin et al., 2019; Yin and Rothenberg, 2016). A condense description of this approach is provided below.

The TCF is defined as Equation (1)

$$f(\mathbf{r_1}, \mathbf{r_2}) = \frac{\langle \delta\rho_1(\mathbf{R})\delta\rho_2(\mathbf{R}+\mathbf{r_1})\delta\rho_3(\mathbf{R}+\mathbf{r_2})\rangle_{\mathbf{R}}}{\langle\rho_1(\mathbf{R})\rangle_{\mathbf{R}}\langle\rho_2(\mathbf{R})\rangle_{\mathbf{R}}\langle\rho_3(\mathbf{R})\rangle_{\mathbf{R}}} \quad (1)$$

where $\langle\rho_i(\mathbf{R})\rangle_{\mathbf{R}}$ denotes the average density of the detections from the *i*th channel within the Region-Of-Interests (ROI, a ~6×6 μm^2 square at the center of the 3-color SMLM image of a nucleus) and $\delta\rho_i(\mathbf{R}) = \rho_i(\mathbf{R}) - \langle\rho_i(\mathbf{R})\rangle_{\mathbf{R}}$ denotes the local density fluctuation at **R**. For coordinate-based binary images, the TCF can be considered to sample the frequency of the triplet Δijk that formed by any given molecule *i*, molecule *j*, and molecule *k* from each of the three different species, respectively (Figure 1C-D(ii), Figure M1B). Each Δijk (as highlighted in Figure M1B for example) is described by the length of its three edges (d_{ij}, d_{jk}, d_{ik}), and all the triplets Δijk can therefore be distributed into 3-D bins corresponding to displacements between Red-and-Blue d_{RB}, Red-and-Green d_{RG}, and Blue-and-Green d_{BG} (Figure M1B(iii)). If the three species are randomly distributed without internal correlation, the frequency of Δijk formed by any stochastic combination of *ijk* can be predicted $\langle\rho_1(\mathbf{R})\rho_2(\mathbf{R}+\mathbf{r_1})\rho_3(\mathbf{R}+\mathbf{r_2})\rangle_{\mathbf{R}} = \langle\rho_1(\mathbf{R})\rangle_{\mathbf{R}}\langle\rho_2(\mathbf{R}+\mathbf{r_1})\rangle_{\mathbf{R}}\langle\rho_3(\mathbf{R}+\mathbf{r_2})\rangle_{\mathbf{R}}$ and subtracted from the 3D distribution (see Supplementary Fig. 2 in Ref. (Yin *et al.*, 2019)). Should the three species form a specific pattern with respect to (w.r.t) a certain $(d_{\mathrm{RG}}, d_{\mathrm{RB}}, d_{\mathrm{GB}})$, it can be then identified from where the 3D distribution distinguishes from 0. Figure M1C and M1D display two scenarios in which the TCF≡ 0 for random distributed three species (Figure M1C) whereas the TCF responds at the certain $(d_{\mathrm{RY}}, d_{\mathrm{RB}}, d_{\mathrm{YB}})$ (Y denotes the *Yellow* species) pattern which are hidden in their chaotic dense distributions (Figure M1D). We note that throughout our studies we have considered several factors that may contribute to the variability of the profiles, including cellular heterogeneity of individual replication forks (Figure 1A and 1B), SMLM 2D projections, the localization and multi-channel mapping accuracy, and cellular perturbation during fixation, though their combined effects was marginal. We also note that these were further minimized by choosing cells in early S-phase (recognized by the relatively homogenous distribution of PCNA across the nucleus) for analyses, and by maintaining identical treatment conditions (cellular fixation, IF staining, etc.) across different experimental sets. As such, the dispersion of the TCF profile was similar for the different experimental sets.

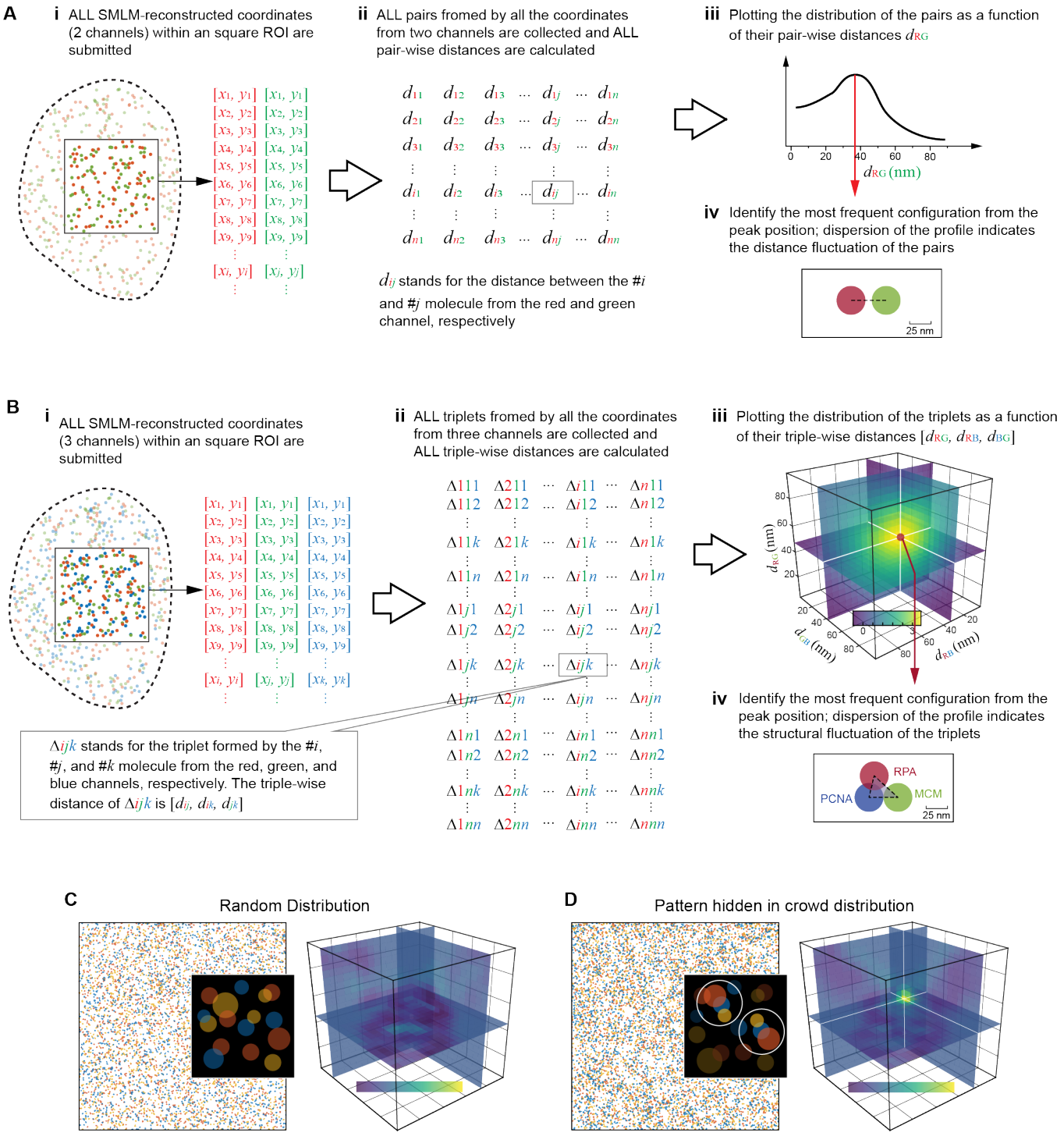

Figure M1. Schematic illustration of data mining via the Triple-Correlation-Function (TCF).

(**A**) Schematic illustration of data mining via Cross-Correlation-Function. Any molecule #i from the red channel and molecule #j from the green channel forms a pair (ii); the pair-wise distances of all the pairs are submitted for frequency count; the distribution of these pairwise distances is plotted as a function of the d_{RG} (iii); the most frequent pair is derived from the peak of the distribution (iv); the dispersion of the distribution indicates the heterogeneity / structural fluctuation of the pairs. (**B**) Schematic illustration of data mining via Triple-Correlation-Function. Any molecule #i from the red channel, molecule #j from the green channel, and molecule #k from the blue channel forms a triplet Δijk (ii), each of which is defined by their triple-wise distances $[d_{ij}, d_{jk}, d_{ik}]$ (the length of its three edges); these triple-wise distances of all the triplets are

submitted for frequency count; the distribution is plotted as a function of $[d_{\mathrm{RG}}, d_{\mathrm{RB}}, d_{\mathrm{GB}}]$ (iii); the most frequent triplet is derived from the peak of the distribution (iv); the dispersion of the distribution indicates the heterogeneity / structural fluctuation of these triplets. (**C** and **D**) Validation of the TCF with simulated data. The randomly distributed species shows TCF ~ 0 across all the 3D-bins (C) whereas the patterns hidden in a chaotic and noisy distribution is identified at their input configuration (D).

Methods S2. Estimation of the local density within a triplet pattern via the TCF

$\langle \delta\rho_1(\mathbf{R})\delta\rho_2(\mathbf{R}+\mathbf{r_1})\delta\rho_3(\mathbf{R}+\mathbf{r_2})\rangle_{\mathbf{R}}$ defines, on average, the product of the local density of the three species within a triplet pattern $\Delta(\mathbf{r_1},\mathbf{r_2})$, while $\langle \delta\rho_1(\mathbf{R})\delta\rho_2(\mathbf{R}+\mathbf{r_1})\rangle_{\mathbf{R}}$ stands for the average product of the two species correlating at $\mathbf{r_1}$. Similar to the joint / conditional probability, the local density of the third species within the triple-pattern is therefore estimated as the 'conditional' local density at $\mathbf{r_2}-\mathbf{r_1}$ given a pair correlating at $\mathbf{r_1}$ (Equation (2)):

$$C_3(\mathbf{r_1},\mathbf{r_2}) = \frac{\langle \delta\rho_1(\mathbf{R})\delta\rho_2(\mathbf{R}+\mathbf{r_1})\delta\rho_3(\mathbf{R}+\mathbf{r_2})\rangle_{\mathbf{R}}}{\langle \delta\rho_1(\mathbf{R})\delta\rho_2(\mathbf{R}+\mathbf{r_1})\rangle_{\mathbf{R}}} \qquad (2)$$

Such local density within a triplet pattern is validated via numerical simulations, in which the TCF-resolved local density of the *Red* indeed only counts for the local density within the triplet patterns (Figure M2A) but not for the changes of the global distribution of the triplet patterns (Figure M2B).

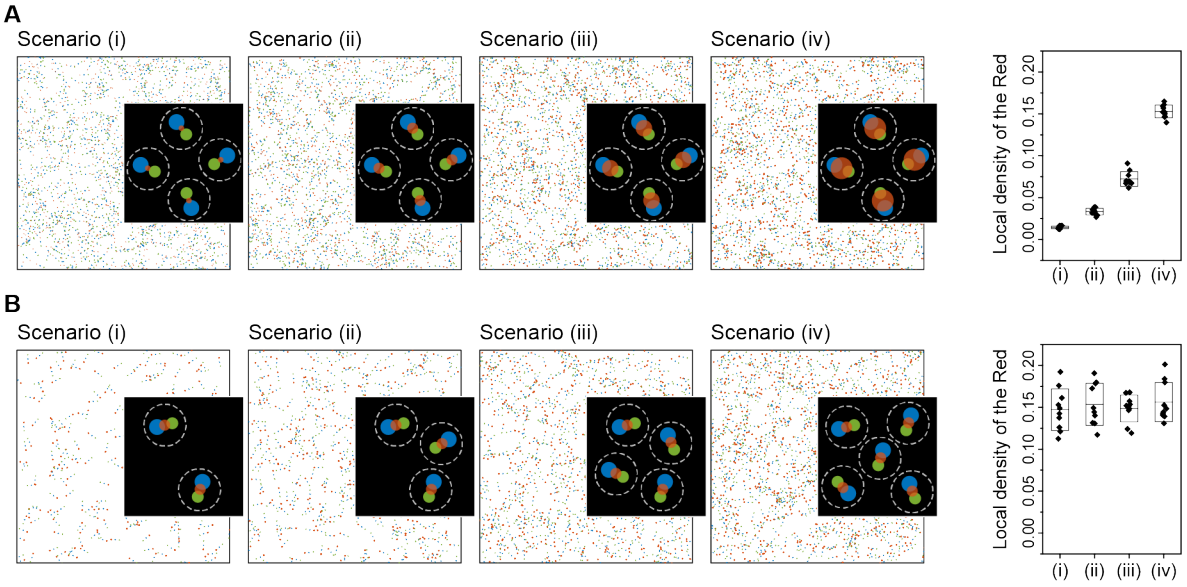

Figure M2. Validation of the robustness of the TCF-resolved local density within a triplet pattern via simulations. (**A**) 1000 triplet BRG patterns were randomly oriented and positioned on the canvas, with each pattern has the same local density of the *Blue* and *Green* but varying local density of the *Red* from scene (i) – (iv), respectively (as schematically illustrated in the zoomed-in region). (**B**) 200 – 800 triplet patterns were randomly orientated and positioned on the canvas from scene (i) – (iv), respectively, with each of the pattern containing the same content of the *Blue*, *Green*, and *Red* (as schematically illustrated in the zoomed-in region). Each scatter in the statistical plots represents the result from 1 simulation. 10 replicas of simulation were performed for each scene in both (A) and (B).

Methods S3. Microscopy System Technical Parameters for Calibration and Aberration Estimation

3.1 Localization Precision and Fourier Correlation Ring

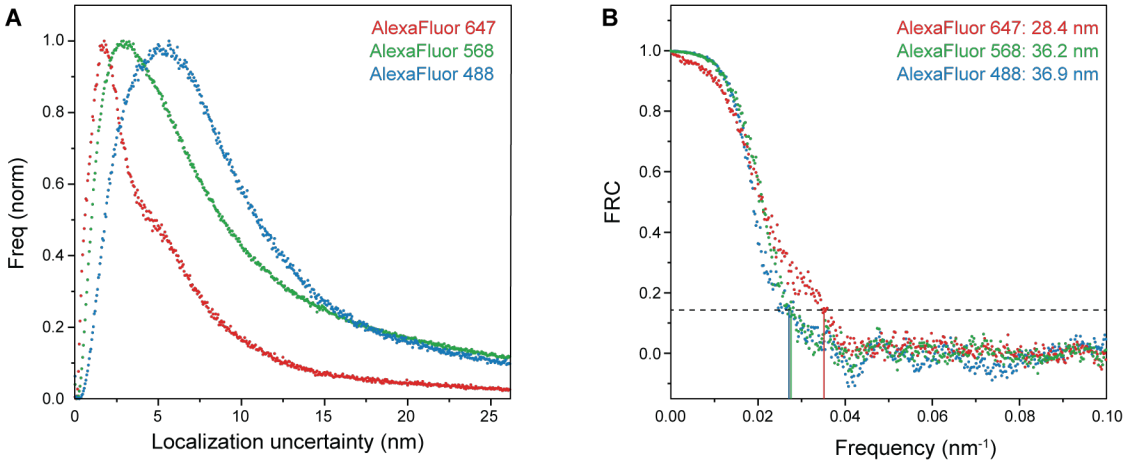

Figure M3. Localization precision and the Fourier Correlation Ring. (**A**) Statistics of the localization accuracy of our SMLM imaging system (the Cramér Rao Lower Bound, CRLB) calculated from a set of Multi-color SMLM experiments. (**B**) The Fourier Correlation Ring profile of a set of Multi-color SMLM experiment. The threshold is set at FRC = 0.143 (1/7) and the cut-off frequency defines the spatial resolution as indicated.

3.2 System Parameters Used for Correction of Axial Chromatic Aberration.

In common practice, correction of the chromatic aberration for 2D images is carried out by the mapping of the pan-spectrum fluorescent beads immobilized on a coverslip glass (STAR Methods). The chromatic aberration could also be z-dependent, as the aberration at a focal plane far away from the coverslip glass might not be appropriately corrected by the on-glass correction map. In addition, the wobble effects(Carlini et al., 2015) within the depth-of-field (dof, ~ 500 – 600 nm for 100x, NA = 1.49 objective used in this work) may also contribute to the aberration. To estimate these errors, we embedded pan-spectrum fluorescent beads in 1% [w/v] agarose gel, and determined their 3D positions, in AF647, AF568, and AF488 channels via a 20 nm-step scanning along the z-axis (the axial position was determined by locating the PSF at its smallest spreading, Figure M4A and M4B).

We first estimated the z-dependent chromatic aberration with a simple model (Figure M4A). We generated the correction map $\mathbf{A}_0$ at the glass $\mathbf{A}_0\mathbf{r}_0^{\text{target}} = \mathbf{r}_0^{\text{ref}}\ (z = 0)$, where $\mathbf{r}_0^{\text{ref}}$ and $\mathbf{r}_0^{\text{target}}$ is the position of a bead in the reference channel (AF647) and the correcting channel (AF568 / AF488), respectively. $\mathbf{A}_0$ was then applied to the beads at varying axial positions $(z = z)$ and the correction error $\Delta\mathbf{r}_z$ was estimated as $\Delta\mathbf{r}_z = \left|\mathbf{r}_z^{\text{ref}} - \mathbf{A}_0\mathbf{r}_z^{\text{target}}\right|$. Figure M4C shows the linear

regression of $\Delta\mathbf{r}_z$ as a function of z of 30 beads, indicating that the on-glass correction may result in an additional 5~15 nm error at a focal plane ~ 2 – 3 μm above the glass.

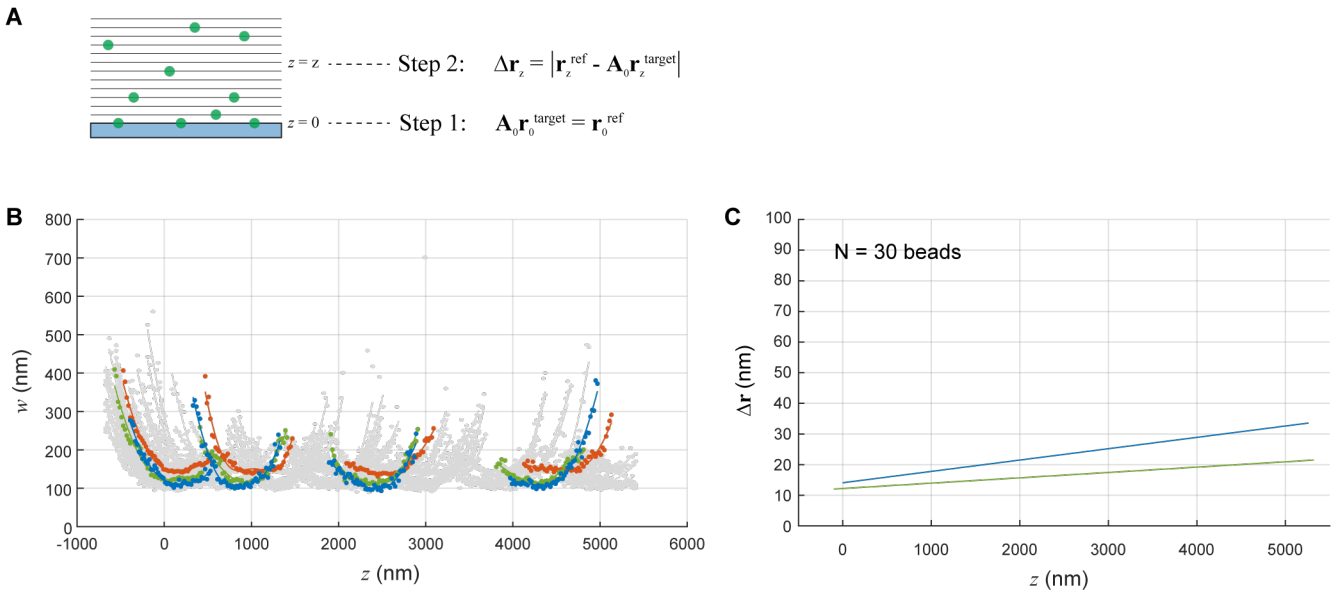

Figure M4. Estimation of the correction error when the on-glass correction is applied to the above-glass focal plane. (**A**) Schematic illustration of the estimation method. (**B**) PSF width (sigma of a 2D gaussian model) of each bead at different z-positions from different color channel. The *w-z* profiles of four representative beads are highlighted. We note that the z-dependent error at the z-axis could also contribute to the x-y- errors (see Fig. M5 for estimation of such errors). (**C**) Linear regression of $\Delta\mathbf{r}_z$ as a function of *z*.

As shown in Figure M4B, when the focal plane is further away from the glass, the chromatic aberration along the z-axis becomes more obvious(Liu et al., 2019), and such z-mismatch may give rise to an additional x-y- error due to the wobble effect(Carlini *et al.*, 2015). To include such error into the z-dependent correction error as indicated above, we formulated the error as a 2D function $\Delta\mathbf{r}(z_1, z_2|z_0) = \left|\mathbf{r}_{z1}^{\mathrm{ref}} - \mathbf{A}_0\mathbf{r}_{z2}^{\mathrm{target}}\right|$ $(z_1, z_2 \in [z_0 - \mathrm{dof}/2,\ \ z_0 + \mathrm{dof}/2])$ where z_0 is the z-position of the focal plane and dof is the depth-of-field (dof was set to 600 nm in the following estimation) (Figure M5A). Figure M5B – M5E display the z-dependent wobble mismatch along x (Figure M5B and M5C) and y (Figure M5D and M5E) axis, between the AF647 channel and the AF568 (Figure M5B and M5D) or the AF488 (Figure M5C and M5E) channel. $\Delta\mathbf{r}(z_1, z_2|z_0)$ of the highlighted beads are shown in Figure M5F. We then use the maximum of $\Delta\mathbf{r}(z_1, z_2|z_0)$ of each bead to estimate the most extreme error that could be brought by the z-dependent chromatic mismatch, and this results in max error of ~ 30 – 40 nm at a focal plane 2 ~ 3 μm above the glass (Figure M5G).

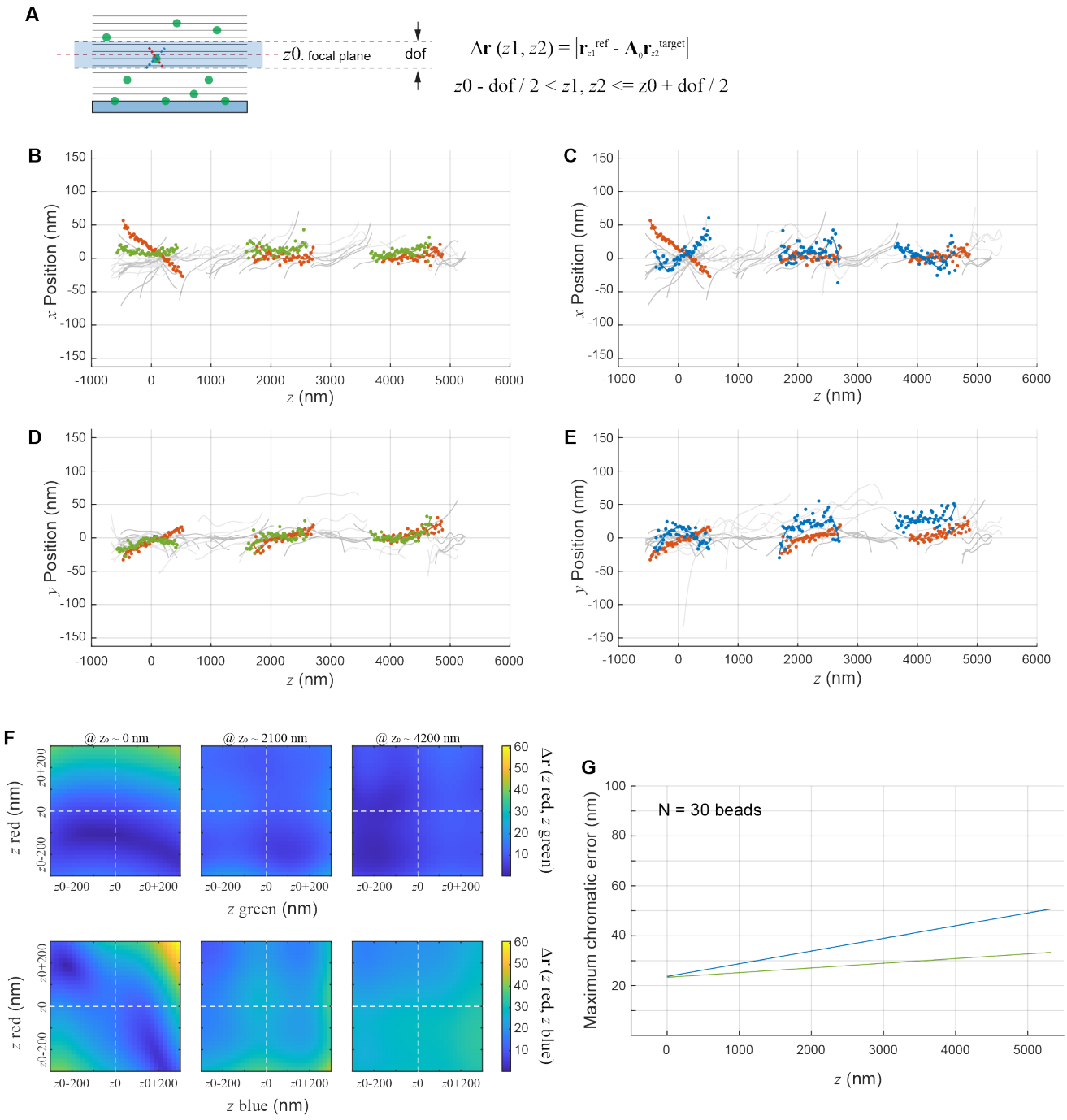

Figure M5. Estimation of the overall z-dependent correction error including the on-glass correction applied to the above-glass focal plane and the wobble-mismatch within the dof. (**A**) Schematic illustration of the estimation formulation. (**B - E**) Wobble mismatch of each bead along x- (B and C) and y- (D and E) axis between AF647 channel and AF568 (B and D) or AF488 (C and E) channels. The wobble profiles from three representative beads are highlighted. (**F**) Heatmap of $\Delta\mathbf{r}(z_1, z_2|z_0) = \left|\mathbf{r}_{z1}^{\text{ref}} - \mathbf{A}_0\mathbf{r}_{z2}^{\text{target}}\right|$ of the three highlighted beads in (B - E). (G) Linear regression of $\max\left(\Delta\mathbf{r}(z_1, z_2|z_0)\right)$ as a function of z_0.

Methods S4. Estimates of the Number of Active Replisomes from SMLM Imaging Data

We utilized correlation-based clustering method (Sengupta *et al.*, 2011; Veatch *et al.*, 2012) to estimate the number of PCNA foci for active replication foci, and the number of MCM foci which includes both active and unfired dormant MCMs, as summarized in Table S1 and shown in Figure S1C-S1E.

The Auto-correlation profile of the examined molecules, for example PCNAs (Figure S1C, black dots) is composed of two levels of correlations; 1) single-molecule blinking events originated from the same fluorophore (Figure S1C, red). This defines the localization uncertainty; 2) fluorophores that labeling the same 'cluster' (Figure S1C, green). This defines the PCNA foci of which the half-width (~40 nm) and number of fluorophores can be derived (Veatch *et al.*, 2012). With this information, the estimated density of active replisomes (PCNA) is ~ 5 per μm^{-2} and chromatin bound MCMs is ~ 10 per μm^{-2}. Assuming one U2OS nucleus is about 10 μm in diameter and 5 μm thick, we estimate the number of active replisomes per nucleus to be ~ 4000 whereas the number of chromatin-bound MCM foci per nucleus was ~ 8000. ATRi treatment induces a little more active foci and a negligible reduction in MCM foci (Figure S1E).

These estimates are comparable to other studies where super-resolution microscopy approaches were used to estimate active replication foci numbers as summarized in Table S1 (Baddeley et al., 2010; Chagin et al., 2016; Cseresnyes et al., 2009; Su et al., 2020). Specifically, Chagin et al estimated the number of replication foci as 4000 – 6000 per cell, whereas Su et al estimates the number of replication foci as ~1600 per cell, whereas our estimate is ~ 3700 per cell. We note that the variability of these estimates might arise not only from the difference in examined cell models but also from the difference in imaging technologies used and also the analyses methods, especially when different thresholding method are applied.